JOURNAL OF GEOPHYSICAL RESEARCH, VOL. 91, NO. C7, PAGES 8411–8427, JULY 15, 1986

Diurnal Cycling: Observations and Models of the Upper Ocean Response to Diurnal Heating, Cooling, and Wind Mixing

JAMES F. PRICE AND ROBERT A. WELLER

Woods Hole Oceanographic Institution, Woods Hole, Massachusetts

ROBERT PINKEL

Scripps Institution of Oceanography, La Jolla, California

Measurements made from R/P *Flip* using rapid profiling conductivity, temperature, and depth probes and vector-measuring current meters provide a new and detailed look at the diurnal cycle of the upper ocean. A diurnal cycle occurs when solar heating warms and stabilizes the upper ocean. This limits the downward penetration of turbulent wind mixing so that air-sea fluxes of heat and momentum are surface trapped during midday. The central problem is to learn how the trapping depth D_T (mean depth value of the diurnal temperature and velocity response) is set by the competing effects of wind mixing and surface heating. In this data set the diurnal range of surface temperature $\tilde{T}_s$ was observed to vary from $0.05 < \tilde{T}_s < 0.4$°C, with most of the day-to-day variability attributable to variations of wind stress τ. Wind mixing causes a pronounced asymmetry of the T_s response by limiting the warming phase to only about half of the period that the surface heat flux Q is positive. The associated wind-driven current, the diurnal jet, has an amplitude of typically $\tilde{V}_s \approx 0.1$ m s^{-1}, with no obvious dependence upon τ. The diurnal jet accelerates downwind during the morning and midday. It is turned into the wind by the Coriolis force during early evening and is often erased by the following morning. Under the assumption that wind mixing occurs as an adjustment to shear flow stability, a scaling analysis and a numerical model study show that the daily minimum trapping depth $\tilde{D}_T$ goes like $\tau/Q^{1/2}$. It follows that $\tilde{T}_s$ goes like $Q^{3/2}/\tau$ and that $\tilde{V}_s$ goes like $Q^{1/2}$. These results, as well as the simulated time dependence of the diurnal cycle, are at least roughly consistent with the observations. The observed time-averaged velocity profile has a spiral shape reminiscent of the classical Ekman spiral. However, its structure is a consequence of diurnal cycling, and its parameter dependence is in some ways just opposite that of the Ekman model; e.g., increased wind stress may cause decreased vertical shear between fixed levels in the upper ocean.

1. INTRODUCTION

A diurnal thermal cycle is well known to occur in the upper ocean whenever the solar heating at midday exceeds the heat loss from the ocean surface [*Sverdrup et al.*, 1942; *Montgomery and Stroup*, 1962; *Tully and Giovando*, 1963; *Stommel et al.*, 1969; *Kondo et al.*, 1979; *Imberger*, 1985]. In the absence of wind effects, solar heating produces strong warming within a very thin surface layer. Under summer heating conditions with vanishing wind, the trapping depth of the thermal response is only about 1 m (mean depth value), and the surface amplitude is as large as 2° or 3°C [e.g., *Halpern and Reed*, 1976; *Stramma et al.*, 1986]. But more commonly, when light or moderate winds are present, solar heating is wind mixed vertically to a considerably greater depth than is reached directly by radiation: the trapping depth is typically $O(10$ m), and the surface amplitude is reduced in inverse proportion to typically $O(0.2$°C) (examples shown here). Given that the surface heating and wind stress are known, then the key to understanding and forecasting the diurnal cycle of the ocean is to learn how the trapping depth is set by the competing effects of a stabilizing surface heat flux and a destabilizing surface stress.

In this paper we take up the diurnal cycle problem by analysis of some new, high-resolution field data and by modeling. Our goals are (1) to describe the temporal and vertical structure of the diurnal cycle and especially the coupling between the thermal and velocity response (section 6); (2) to develop a simple numerical model of the upper ocean response to heating and wind mixing which can simulate the diurnal cycle (sections 4 and 7); (3) to determine the explicit parameter dependence of the diurnal cycle upon the heating rate, the wind stress, and other external variables (sections 5 and 7), and lastly (4) to show how the process of diurnal cycling acts to shape the longer term response of the upper ocean to atmospheric forcing (section 8).

Paper number 6C0214
0148-0227/86/006C-0214$05.00

2. FIELD OBSERVATIONS

The field data reported here were taken in spring 1980 from R/P *Flip*. Measurements were begun on April 28 at 30.9°N, 123.5°W, about 400 km west of San Diego, California. *Flip* drifted southward with the prevailing wind, and the measurement program ended on May 24 when *Flip* was at 28.7°N, 124.0°W.

2.1. *Data Types*

The major strength of this data set is that it includes vector-measuring current meter (VMCM) velocity measurements from a stable platform [*Weller and Davis*, 1980], along with rapid profiling conductivity, temperature, and depth (CTD) measurements [*Pinkel*, 1975]. Hence for apparently the first time it is possible to describe the joint response of velocity and temperature over a diurnal cycle. The usual shipboard meteorological measurements were also made, including direct measurements of solar insolation (sampling intervals and estimates of precision for each of the measurements are in Table 1). *Weller* [1985] presents a complementary analysis of the thermocline-depth inertial motions observed in this data set, and *Pinkel* [1983] describes the thermocline-depth internal wave field observed with Doppler sonar.

TABLE 1. *Flip* 1980 Data Base

Type	Sampling Range	Sampling Interval	Precision	Comments
profiling CTD; T, C, P	$128.4 < t < 145.3$ days* $2 < z < 400$ m	$\Delta t = 2$ min $\Delta z = 1$ m	$T \pm 0.002$°C $C \pm 0.2$ $z \pm 1$ m	some intermittent recorder drop-out
profiling VMCM; V, T, P	$119.7 < t < 145.2$ $6 < z < 150$ m	$\Delta t = 30$ min† $\Delta z = 4$ m	V ± 0.01 m s^{-1} $T \pm 0.02$°C $z \pm 1$ m	gap on 133 due to servicing
Fixed level VMCM; V, T	$119.7 < t < 145.2$ $z = 2$ m	$\Delta t = 1$ min	as above	as above
Wind speed U	$119.2 < t < 145.3$ $z = 22$ m above sea level	$\Delta t = 30$ min	$U \pm 1$ m s^{-1}	
Eppley pyranometer, I_0	as above	as above	$\pm 5\%$	
Air temperatures, cloud cover, pressure	as above	as above	± 1°C; ± 2 oktas; ± 1 mbar	

*Times are given in local year days, i.e., 120.5 was local noon on 29 April.

†All VMCMs sampled once per minute. The profiling VMCMs made one profile every 30 min. Velocity from the profiling VMCMs was collected while they were moving and is thus an average over 1 min and over a vertical distance of $\simeq 2$ m.

The profiling VMCMs and CTD were operated automatically. The CTD was brought as close to the mean sea surface as possible, ~ 1 m, without breaking the surface at the troughs of swell which had an amplitude of about 1 m. The profiling VMCMs were brought to within $\simeq$ 6 m of the surface, and a fixed-level VMCM was set at $\simeq$2-m depth. The shallowest depth sampled consistently was thus 2 m below the mean sea surface. We call the 2-m temperature T_s, for near-surface temperature, to distinguish it from the literal sea surface temperature, which might be slightly cooler on account of skin effects or warmer if the upper meter becomes stratified under extremely light wind conditions [*Bruce and Firing*, 1974; *Soloviev and Vershinsky*, 1982].

2.2. *Meteorology and Air-Sea Fluxes*

The North Pacific high dominated the weather over most of the eastern North Pacific during the time of this experiment, and the weather observed at *Flip* was consistently fair. Wind direction was toward southeast to southwest for the entire 25-day measurement period, while wind speed U varied from 3 to 12 m s^{-1}. Wind stress τ was calculated as

$$\tau = \rho_a C_D U \mathbf{U}$$

where $\rho_a = 1.23$ kg m^{-3} is the density of air and C_D is the drag coefficient computed by the *Large and Pond* [1981] formulation (the neutral 10-m C_D was in the range 1.3–1.6 $\times 10^{-3}$). The estimated wind stress varied by an order of magnitude from 0.02 to 0.25 N m^{-2} (Figure 1*b*) and changed at intervals of typically 2 to 4 days; there were four periods of relatively strong wind stress (days 120–122 and 127–129 and to a lesser degree, days 135–137 and 144–145) and two periods of very weak stress (days 123–127 and 132–135). As we will see in section 7, this several day period modulation of wind stress magnitude is strongly impressed on the diurnal thermal cycle.

The surface heat flux, $Q = I + L$, is the sum of solar insolation I, which was directly measured, and heat loss L, which is itself the sum of latent, sensible, and long-wave radiative heat fluxes. These were calculated from the air-sea observations using the *Large and Pond* [1982] bulk formulation, and standard radiation formulae [*Kraus*, 1972, equation 3.35]. The daily maximum I varied from roughly 500 W m^{-2} on days when cloud cover was nearly complete to roughly 1000 W m^{-2} on clear days (Figure 1*a*). Heat loss varied from about -100 to -300 W m^{-2} depending upon wind speed and humidity.

On each day of this experiment Q was positive (warming) during midday, and hence there was an oceanic diurnal cycle of some sort on each day. This data set samples a fairly wide range of heating and wind stress conditions, $400 < Q < 900$ W m^{-2} and $0.02 < \tau < 0.25$ N m^{-2}, and thus we have an opportunity to learn here how these day-to-day variations of Q and τ affect the diurnal cycle.

2.3. *Overview of the Data*

VMCM temperature measurements sampled as time series at depths of 2, 10, 15, 20, and 25 m (Figure 1*c*) provide an overview of this data set and some perspective on the diurnal cycle. By far the most energetic signal seen here is an irregular low-frequency fluctuation of temperature which at first glance seems to swamp the diurnal cycle and any local effect of air-sea heat exchange (Figure 1*d*). These low-frequency changes of temperature and heat content are probably due mainly to horizontal advection of mesoscale variability, which can be strong in this region [*Lynn and Svejkovsky*, 1984]. (For example, the rapid increase of temperature that occurred late on day 134 was nearly uniform through the upper 40 m and so cannot be due to vertical advection, and it was much larger than any possible effect of local air-sea heat exchange.) Velocity records have much the same character; the low-frequency currents that accompany this advection, plus tides, inertial motions, and internal waves [*Weller*, 1985; *Pinkel*, 1983], often overwhelm the diurnal cycle of wind-driven velocity. Fortunately there was a several-day period, days 128–131, when the heat budget suggests that advective effects were relatively weak. CTD and VMCM data from this period will be examined in particular detail.

2.4. *Vertical Anomalies*

Though the diurnal variability in temperature or velocity is comparatively small, note that the variability of stratification

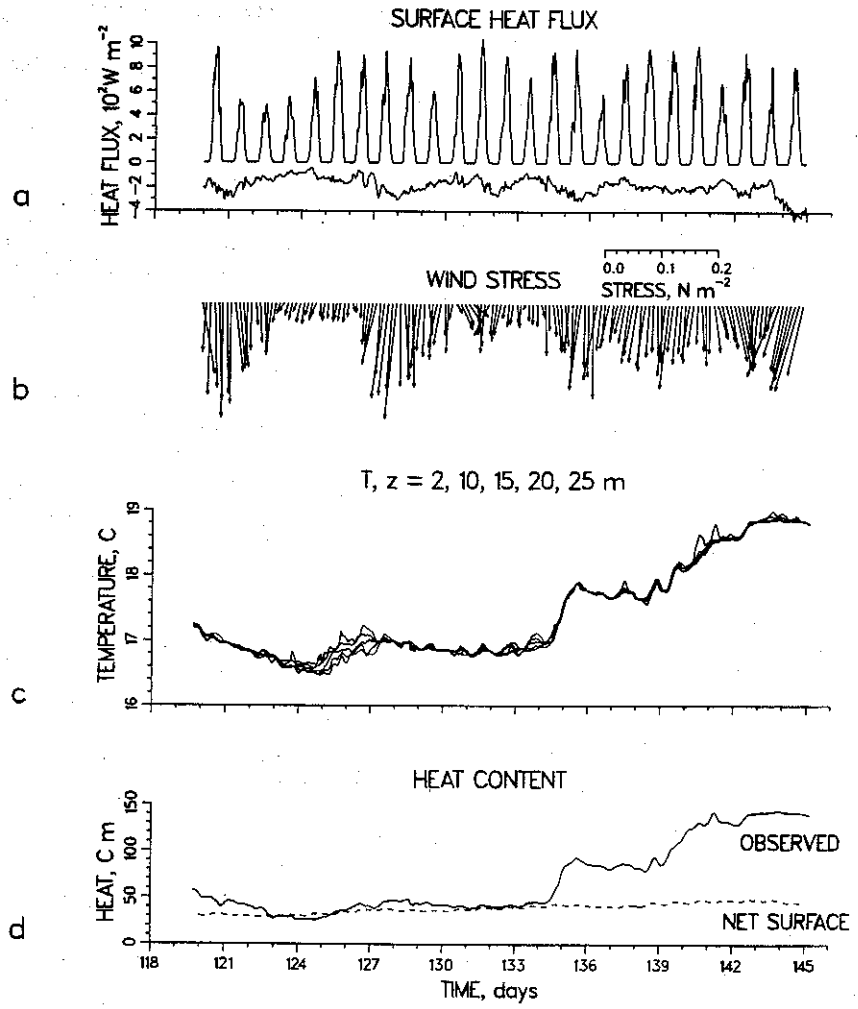

Fig. 1. Air-sea fluxes and overview of the temperature observations. (*a*) Heat fluxes. Insolation I (upper line) was directly measured; heat loss L (lower line) was computed from air-sea measurements using standard methods. (*b*) Wind stress computed from the observed wind using the bulk aerodynamic method. North is up. (*c*) VMCM-measured temperature time series at depths of 2, 10, 15, 20, and 25 m. (*d*) Observed heat content in the upper 40 m (solid line), and the integrated air-sea heat flux (dashed line). Note that the rate of change of observed heat content differs greatly from the air-sea flux (presumably because of advection) except during a several-day period around 130.

(temperature difference from 2 to 25 m, say) is generally dominated by the diurnal cycle. The same is true for the vertical shear of the horizontal velocity. Hence one simple, and fairly effective way to separate out the signal of the diurnal cycle is to compute the temperature and velocity vertical anomalies,

$$T'(z, t) = T(z, t) - T(z_r, t)$$

$$\mathbf{V}'(z, t) = \mathbf{V}(z, t) - \mathbf{V}(z_r, t)$$

where the reference level z_r should (1) be in a vertically homogeneous layer to escape the effects of vertical advection and yet (2) be deep enough that the diurnal cycle amplitude at z_r is negligible. On days 128–131 a reference depth $z_r = 40$ m roughly satisfies conditions 1 and 2 above. For the record as a whole, there is no single suitable reference depth, and hence when dealing with the full record we are forced to work with stratification and shear (vertical differences over depths of less than the ideal z_r) rather than temperature and velocity anomalies.

3. Diagnostic Length Scales

To describe the structure of the observed temperature and velocity profiles we will use the familiar jargon "mixed layer" to denote a quasi-homogeneous surface layer (temperature uniform to within 0.02°C, velocity to within 0.01 m s^{-1}) and "transition layer" to denote the stratified layer between the mixed layer and undisturbed fluid beneath [e.g., *Price*, 1979]. These are useful descriptive terms but are not always suitable for defining quantitatively a profile structure. As just one example, on days with strong winds the upper ocean may be only very weakly stratified, and the mixed layer depth estimated from field data can be quite sensitive to the somewhat arbitrary degree of homogeneity which defines the mixed layer.

At some risk of confusion we therefore suggest two new length scales to measure the depth of surface trapping and the depth of mixing. These length scales have the advantages of being model independent and parameter free, and they can be objectively estimated from field and model data. Both require a profile of the temperature anomaly T'.

"Trapping depth" D_T is defined as the mean depth value of the temperature anomaly profile,

$$D_T = \frac{1}{T_s'} \int_{z_r}^{z_s} T'\, dz \qquad (1)$$

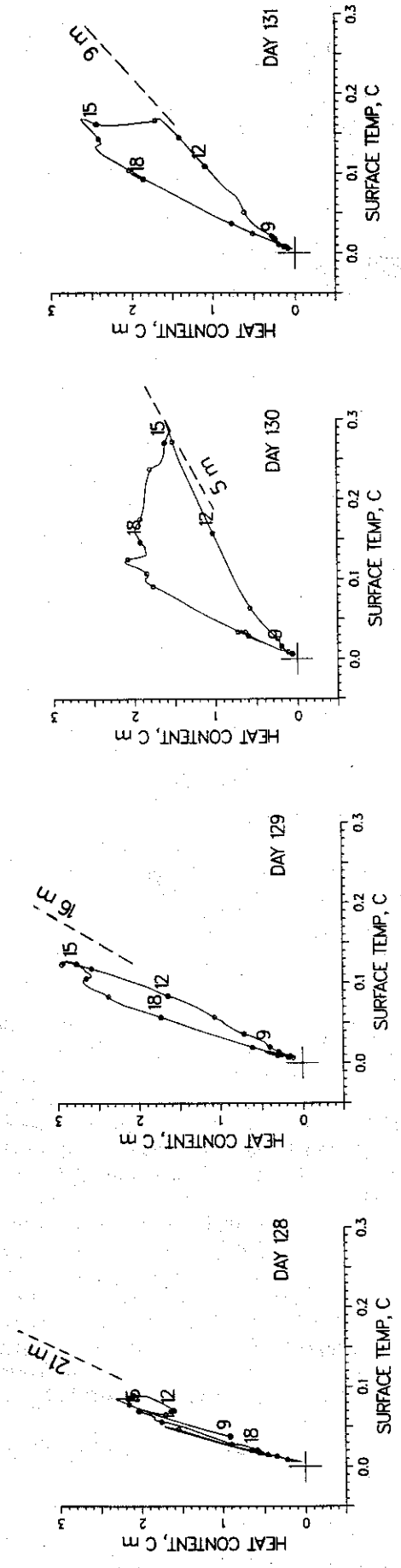

Fig. 2. Heat content plotted as a function of near-surface temperature for each of days 128–131. Local time in hours is marked along the curves. The daily minimum trapping depth estimated from Figure 6*e* is shown as a dashed sloping line.

where in our case $z_r = 40$ m, and $z_s = 2$ m. In those profiles where a mixed layer/transition layer structure is well defined, then D_T will lie near the middle of the transition layer. This trapping depth may be evaluated over each individual CTD-observed or model-computed profile.

"Penetration depth" D_P is defined as the length scale $(\partial/\partial z)^{-1}$ of the one-dimensional heat equation, $\partial T/\partial t = (-1/\rho_0 c)\ (\partial F/\partial z)$, where ρ_0 and c are the density and heat capacity of sea water (both constant), and F is the heat flux whose surface value is Q. Penetration depth is estimated here as the surface value of the length scale,

$$D_P = \frac{Q}{\rho_0 c \partial T_s'/\partial t} \tag{2}$$

During the rising phase of the heating cycle when the heat flux profile is monotonically decreasing with depth (section 6), D_p is a direct measure of the depth of wind mixing.

Both D_T and D_P may be written in terms of the heat content, H (kinematic units), of the temperature anomaly profile,

$$H = \int_{z_r}^{z_s} T'\, dz$$

Obviously,

$$D_T = H/T_s'$$

which makes clear that for a given H (which is imposed externally), the surface thermal response is inversely proportional to the trapping depth. In the absence of advection, $\partial H/\partial t = Q/\rho_0 c$, and then

$$D_P = \frac{\partial H}{\partial T_s'}$$

These suggest plotting H versus T_s' hysteresis curves for the diurnal cycle (Figure 2) the way *Gill and Turner* [1976] did for the seasonal cycle. On most days the hysteresis curves grow almost straight out from the origin until a few hours after noon when they begin to turn counterclockwise (increasing heat content and decreasing surface temperature). The daily minimum values, $\tilde{D}_T$ and $\tilde{D}_p$, are thus nearly equal on most days (this need not be true in general).

Note that between these four successive days there is roughly a factor of 4 difference in $\tilde{D}_T$ (or $\tilde{D}_p$) and a corresponding difference in the amplitude of T_s'. As we suggested in the introduction, the key to understanding the diurnal cycle is to learn how these important day-to-day changes in the trapping depth depend upon the day-to-day variability in the heating and wind stress.

4. A Model of the Upper Ocean Response to Heating and Wind Mixing

4.1. *Budgets*

The diurnal cycle is modeled as a vertical mixing and radiation process driven solely by the local surface fluxes of heat and momentum [e.g., *Niiler and Kraus*, 1977]. We are thereby assuming that the diurnal cycle rides passively and noninteractively on top of the ambient oceanic variability. Under this assumption the budget equations for the diurnal cycle are the usual one-dimensional forms:

$$\frac{\partial T}{\partial t} = \frac{-1}{\rho_0 c}\frac{\partial F}{\partial z} \tag{3}$$

$$\frac{\partial S}{\partial t} = -\frac{\partial E}{\partial z} \tag{4}$$

$$\frac{\partial \mathbf{V}}{\partial t} = -\mathbf{f} \times \mathbf{V} - \frac{1}{\rho_0}\frac{\partial \mathbf{G}}{\partial z} \tag{5}$$

where the flux profiles are to be determined. The surface values are presumed known: $F(0) = Q$, the air-sea heat flux, positive downward; $E(0) = S(E - P)$, the freshwater flux times surface salinity; and $\mathbf{G}(0), = \tau$, the wind stress.

The heat loss L is presumed to leave directly from the sea surface, while solar insolation is absorbed within the water column with a double exponential depth dependence [*Kraus*, 1972],

$$I(z) = I(0)[I_1 \exp(-z/\lambda_1) + I_2 \exp(-z/\lambda_2)] \tag{6}$$

Subscripts 1 and 2 refer to the shortwave and long-wave components of insolation, and z is positive downward with $z = 0$ being the sea surface. *Paulson and Simpson* [1977] provide the parameters of (6) for a wide range of oceanic water types. In the case of fairly clear, mid-ocean water (type 1A), which we assume holds for our measurement site in the open subtropical Pacific (30°N, 124°W),

$$I_1 = 0.62 \qquad \lambda_1 = 0.6 \text{ m}$$

$$I_2 = 1 - 0.62 \qquad \lambda_2 = 20 \text{ m}$$

and thus about half of the solar insolation is absorbed within the uppermost meter of the water column. The remaining shortwave component of the insolation is absorbed with an extinction scale of 20 m.

Absorption of radiation in the water column would by itself yield a trapping depth of about 2 m. The observed trapping depth is usually much greater, $O(10 \text{ m})$, showing that the heat flux profile $F(z)$ is usually determined more by wind mixing than by radiation absorption alone.

Density is calculated from a linear state equation,

$$\rho = \rho_0 + \alpha(T - T_0) + \beta(S - S_0) \tag{7}$$

where in this case $\rho_0 = 1.025 \times 10^3$ kg m^{-3}, $T_0 = 17$°C, $\alpha = -0.23$ kg m^{-3} °C^{-1}, $S_0 = 36$ parts per thousand (ppt), and $\beta = 0.76$ kg m^{-3} ppt^{-1}.

4.2. *Mixing*

The only artful part of such a model is its parameterization of wind mixing. We have experimented with a fairly broad range of mixing parameterizations (with help from P. Martin and P. Klein) and present the model which appeared to us to have the most realistic parameter dependence and profile structure (see *Martin* [1986] for extensive model comparisons). This model is essentially the dynamic instability model (DIM) mixed-layer model of *Price et al.* [1978] (see also *Pollard et al.* [1973] and *Kronenburg* [1985]) which is modified here by including a mixing process in the stratified fluid below the mixed-layer.

Vertical mixing occurs in this model in order to satisfy stability criteria which require that

$$\frac{\partial \rho}{\partial z} \geq 0 \tag{8}$$

for static stability,

$$R_b = \frac{g\Delta\rho h}{\rho_0(\Delta \mathbf{V})^2} \geq 0.65 \tag{9}$$

for mixed layer stability, and

$$R_g = \frac{g\partial\rho/\partial z}{\rho_0(\partial \mathbf{V}/\partial z)^2} \geq 0.25 \tag{10}$$

for shear flow stability. In the mixed-layer criterion (9), h is the mixed-layer depth, and $\Delta(\ )$ takes the difference between the mixed layer and the level just beneath.

In Appendix A we describe some model experiments that show the consequences of each of these three mixing processes. Briefly, the first mixing process simulates free convection, which occurs whenever there is heat loss from the sea surface (always in this data set). Free convection will cause mixing down to the convection depth [*Dalu and Purini*, 1981], which is quite shallow for the range of τ and Q encountered in this study, typically < 1 m at midday. The second mixing process simulates mixed-layer entrainment by relaxation of an overall Richardson number, and the third mixing process simulates the effects of shear flow instability by relaxation of the gradient Richardson number. These latter two are by far the dominant vertical mixing processes for the τ, Q range of this study and are emphasized throughout. They may be regarded as wind-mixing processes in the sense that the velocity which appears in the Richardson numbers is entirely wind driven, and both processes would be inactive if the wind vanished. Our motivation for using both a bulk and a gradient mixing process is discussed in the subsection below, in section 7, and in Appendix A.

4.3. *Implementation*

The model is set up on a high-resolution vertical grid, $\Delta z = \frac{1}{2}$ m, and run with time steps $\Delta t = 900$ s. At each time step solar insolation is absorbed according to (6), and the air-sea heat loss L and freshwater flux $E - P$ are extracted from the topmost grid level. The density profile is then calculated and if necessary adjusted to achieve static stability (equation (8)) by mixing from the surface downward to simulate free convection. The heat flux profile accompanying free convection is [see *Deardorff et al.*, 1969],

$$F(z) = F(0)(1 - z/h) \tag{11}$$

Wind stress is then absorbed within the mixed layer, the momentum balance is stepped forward in time, and the mixed-layer Richardson number R_b calculated. If $R_b < 0.65$, then the mixed layer entrains successively deeper levels until (9) is satisfied. The heat flux profile that accompanies this wind-mixing process increases from the surface downward, has a maximum at the depth of the mixed layer,

$$F(z) = -\frac{z}{h}\Delta T \frac{dh}{dt} \tag{12}$$

and vanishes below. Similar terms appear in the salinity and momentum budgets.

To this point the model is exactly the DIM model of *Price et al.* [1978], and like all conventional, bulk, mixed-layer models [e.g., *Denman*, 1973] it assumes the existence of a surface mixed layer having a jump of density and velocity at its base. The field data shown here make clear that while a surface mixed layer is well included in an upper ocean model, there is certainly no sharp jump at its base. Instead, there is a smooth (at the several-meter scale), and sometimes quite thick transition layer across which the mixed-layer temperature and velocity match with the fluid below. This transition layer is a

major feature of the observed profiles which has to be simulated in the model before it is plausible to make a direct comparison with field data.

Guided in part by the observations of *Price* [1979] (see references therein to atmospheric boundary layer studies) and by the presumption that sharp jumps are likely to be the sites of shear flow instability, we have gone on to require that the gradient Richardson number R_g be no less than a presumed critical value, 0.25 [*Turner*, 1973; *Thompson*, 1980; *Adamec et al.*, 1981]. R_g is calculated by first differences over the stratified part of the profile (not in the mixed layer). If the smallest R_g in the profile is found to be less than the presumed critical value of 0.25, then ρ, T, S, and $\mathbf{V}$ at the two grid levels that produce the smallest R_g, say, j and $j+1$, are partially mixed according to

$$\rho_j' = \rho_j - \left(1 - \frac{R_g}{R_g'}\right)(\rho_j - \rho_{j+1})/2$$

$$\rho_{j+1}' = \rho_{j+1} + \left(1 - \frac{R_g}{R_g'}\right)(\rho_j - \rho_{j+1})/2$$

where $(\ )'$ is the value after mixing. $R_g' = 0.3$ is a specified constant which is set just slightly larger than the critical value to hasten convergence. (The choice $R_g' = 0.3$ versus, say, 0.25 is strictly for numerical convenience and has no appreciable consequence in the solutions.) R_g is then recalculated from $j-1$ to $j+2$, and the search and mixing procedure continues until $R_g \geq 0.25$ throughout the stratified portion of the profile. The effect on the heat flux profile (equation (12)) is to smear out the otherwise sharp corner at $z = h$ produced by mixed-layer entrainment.

5. Scale Analysis

One of the primary goals of this paper is to learn the explicit parameter dependence of the diurnal cycle. Given that we do not know an analytic solution of our model when heating is applied, we attempt to deduce the parameter dependence by a scaling and dimensional analysis.

The analysis is simplified a good deal in the case when, as commonly occurs, nighttime cooling and wind mixing produce an early morning mixed layer which is somewhat deeper than the trapping depth of the coming day. The new diurnal cycle is then written upon a "clean slate" [*Stommel et al.*, 1969] which has no important memory of the previous day's stratification or velocity. The external parameters which control the diurnal cycle are then those that describe the atmospheric forcing plus rotation.

For simplicity, the surface heat flux is taken to be made up of a steady heat loss L and a sinusoidal insolation I (for now assumed absorbed at the surface, i.e., $\lambda_1 = \lambda_2 = 0$). The time scale of the heating, P_Q, is defined as half of the interval during which $Q > 0$.

5.1. *Temperature and Velocity Anomalies*

Assuming for the moment that the trapping depth D_T is known, then from the heat equation (3) we can immediately write down estimates of the temperature and density anomalies,

$$\delta T \sim \frac{QP_Q}{D_T \rho_0 c} \tag{13}$$

and from (7),

$$\delta\rho = \alpha \delta T \tag{14}$$

The coefficient required to make an equality in (13) is $O(1)$ but will remain unknown until the scale analysis results are calibrated against the numerical model.

Wind stress is assumed to be steady with amplitude τ and, like the heat flux, to be trapped over a depth D_T during a time interval proportional to P_Q. The velocity anomaly is then given by the Fredholm solution [*Phillips*, 1977],

$$\delta V \sim \frac{\tau}{D_T f \rho_0} [2 - 2\cos(ft)]^{1/2}$$

where $t = 0$ is the start of heating. (It is easy to show that the velocity anomaly is independent of the velocity left over from the preceding day [*Price*, 1979]). Further discussion of the scale analysis is limited to cases in which the heating time scale P_Q is less than half the local inertial period. This effectively limits the scale analysis to low and middle latitudes where diurnal cycling is most important (and excludes the nonetheless interesting case of high-latitude summer where the diurnal variability of heating gives way to a seasonal variability). For the purpose of determining D_T the relevant velocity anomaly is that which occurs at about local noon, or $t = P_Q$. It is convenient to define an acceleration time scale, P_τ, which accounts for rotation,

$$P_\tau = \frac{1}{f}[2 - 2\cos(fP_Q)]^{1/2}$$

and rewrite the velocity anomaly in the more compact form

$$\delta V \sim \frac{\tau P_\tau}{D_T \rho_0} \tag{15}$$

For a given D_T these estimates of the temperature and velocity anomalies follow directly from the budgets (equations (3)–(5)) and should obtain for any one-dimensional model. However, the dependence of D_T upon Q and τ can vary greatly between different mixing parameterizations and hence so too will the dependence of δT and δV.

5.2. *Trapping Depth*

The notion behind our model is that wind mixing occurs primarily to relieve shear flow instability. The stability limit is given by a Richardson number criterion, and it might be guessed that a relation like (9) should obtain between the density and velocity anomalies and the length scale D_T. Substitution of (14) and (15) into (9) to solve for D_T in terms of the external variables τ and Q, then gives the scale analysis result that

$$D_T \sim \frac{\tau}{Q^{1/2}} \frac{P_\tau}{P_Q^{1/2}} \left(\frac{c}{-\alpha g}\right)^{1/2} \tag{16}$$

Elimination of D_T from (14) and (15) gives

$$\delta T \sim \frac{Q^{3/2}}{\tau} \frac{P_Q^{3/2}}{P_\tau} \frac{(-\alpha g)^{1/2}}{\rho_0 c^{3/2}} \tag{17}$$

$$\delta V \sim Q^{1/2} \frac{P_Q^{1/2}}{\rho_0} \left(\frac{-\alpha g}{c}\right)^{1/2} \tag{18}$$

Numerical experiments have verified that this is indeed the parameter dependence of our model. We expect it will hold for other models whose mixing parameterization depends upon a mean flow Richardson number [e.g., *Mellor and Durbin*, 1975;

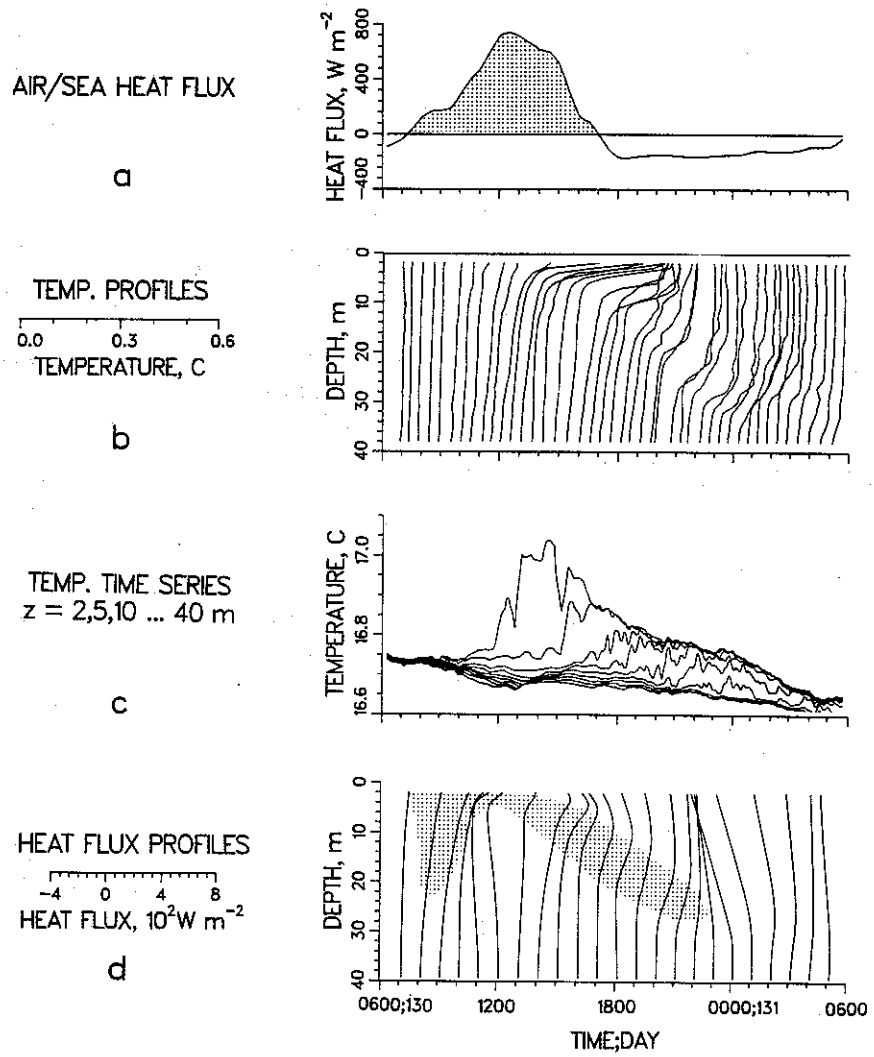

Fig. 3. Diurnal thermal cycle observed on day 130. (*a*) Air-sea heat flux. The heating period is shaded. (*b*) Temperature profiles measured by rapid profiling CTD. Time is to be read from the bottom of the profiles. Note that the upper 2 m was not sampled. (*c*) Temperature time series at depths of 2, 5, 10, ···, 40 m. (*d*) Heat flux profiles calculated from the observed rate of change of temperature. Regions of warming are shaded.

Dickey and Simpson, 1983; *Kondo et al.*, 1979], but probably not those models built upon Monin-Obukhov scaling [e.g., *Gill and Turner*, 1976; *Garwood*, 1979; *Davis et al.*, 1981; *Woods and Barkmann*, 1986] or the classical diffusion model. (Under the assumption that no external time scale is relevant for determining D_T, then dimensional analysis leads directly to the Monin-Obukhov scaling $D_T \sim \tau^{3/2}/Q$ [*Turner*, 1973]. From (13) and (15), $\delta T \sim Q^2/\tau^{3/2}$ and $\delta V \sim Q/\tau^{1/2}$, which can be quite different from (16)–(18). In particular, note that for a given range of Q and τ the Monin-Obukhov scaling will give a larger range of δT than does (17).)

In Appendix B the basic scaling results (equations (16)–(18)) are developed further by accounting for (1) radiation absorption at depth, (2) the constants needed to make equalities, and (3) the limit of vanishing τ.

6. Description of the Diurnal Cycle

To illustrate the structure of the diurnal cycle, we have chosen two particularly clean and representative examples for a close look: the large-amplitude thermal cycle on day 130, which had light and somewhat variables winds, and the velocity cycle on day 131, which had fairly steady wind and also had an appreciable thermal response. The full 25-day record is then used to show the coupling between the thermal and velocity cycles and to begin to consider the day-to-day variability of the diurnal cycle.

6.1. *Thermal Cycle*

It is helpful to describe the thermal cycle partly in terms of the heat flux profile which is calculated by integrating the heat equation (3) upward from the reference depth [*Deardorff et al.*, 1969],

$$F(z) = \rho_0 c \int_{z_r}^{z} \frac{\partial T'}{\partial t}\, dz$$

Heat flux profiles estimated from field data in this way are easily contaminated by horizontal and vertical advection and cannot in all cases be interpreted as the consequence of a local, vertical mixing or radiation process. However, the three main stages of the thermal cycle described below from day 130 occur repeatedly in the data and are thought to be genuine signals of the diurnal cycle.

Stage 1: *Warming throughout.* From sunrise until about

noon, the heat flux profile decreases monotonically from the surface as warming occurs throughout the water column (Figure 3). So long as the heat flux profile is monotonic, its decay scale can be measured by the penetration depth D_P (section 3). D_p usually reaches a daily minimum value at around noon and on day 130 is fairly shallow, $\tilde{D}_p \simeq 5$ m. Levels above 5 m thus warm rapidly during midday, while at the same time the heat flux is effectively cut off from deeper levels, >15 m, which remain at a nearly constant temperature throughout the morning (aside from some very weak warming by direct absorption of radiation evidenced by the smooth increase in stratification between 15 and 40 m).

Stage 2: Cooling and warming. Starting within a few hours after noon, wind mixing begins to mix downward the heat stored near the surface during midday and causes the heat flux profile to develop a distinct knee, or middepth maximum (equation (12)). The knee in the heat flux profile corresponds closely to the depth of the deepening surface mixed layer. Above the knee, or within the mixed layer, this wind mixing causes rapid cooling during the early afternoon, even while the surface heat flux remains fairly strong and positive. Wind mixing thus causes a rather pronounced asymmetry in the response of surface temperature by limiting surface warming to just a little more than a quarter of the day (observed also by *Hoeber* [1972] and *Dickey and Simpson* [1983]).

Below the knee and over a depth that corresponds roughly to the upper portion of the transition layer, vertical wind mixing causes warming. Continued wind mixing pushes the knee downward through the water column during the late afternoon and early evening. When the thermal response is strongly surface trapped, as it was on this day, then at middepths, 20–30 m, the warming phase of the diurnal cycle may be very abrupt, lasting only the few hours required for the passage of the heat flux knee and the associated transition layer. Cooling begins at a given level immediately after the knee passes, and along with the arrival of the mixed-layer.

Stage 3: Cooling throughout. By about midnight, the downward propagation of the heat flux knee has reached to 30 m depth. Thereafter, the heat flux profile is dominated by the heat loss to the atmosphere and again becomes monotonic, with cooling throughout the depth of the mixed layer (equation (11)). Heat loss continues until the following sunrise and erases the heat anomaly from day 130 before the warming phase of the thermal cycle reaches below 35 m.

6.2. *Diurnal Jets and the Velocity Cycle*

The diurnal cycle has a profound effect upon the wind-driven velocity. It produces a characteristic mode of variability that we have dubbed the "diurnal jet" [*Weller et al.*, 1983] and sets the vertical structure of the time-averaged, wind-driven transport (described in section 8).

A diurnal velocity cycle comes about because heat and momentum are mixed in what appears to be a similar way, i.e., the penetration depth for the momentum flux shoals during midday right along with the penetration depth for the heat flux discussed above. (This was first suggested for the ocean by *Montgomery and Stroup* [1962]; see also *Kondo et al.* [1979]. For description of the nocturnal jet of the planetary boundary layer, see *Gill* [1982], *Thorpe and Guymer* [1977], and also *Rubenstein* [1981]). In addition, the wind-driven velocity is subject to the Coriolis force, which turns the velocity vector cum sole (clockwise) during the day. The diurnal velocity cycle thus has some of the character of the inertial motion solution to the Fredholm problem. In that case the wind stress is time dependent; in this case the wind stress is steady (or may be so imagined), but the stress penetration depth varies as part of the diurnal cycle.

An example of the diurnal velocity cycle is shown in Figure 4, where VMCM-measured velocity is shown as vectors at depths of 2, 5, 10, 15, $\cdots$, 40 m. Velocity is referenced to 40 m in an attempt to suppress the competing velocity signals from tides and ambient inertial and geostrophic motions [*Weller*, 1985; *Pinkel*, 1983]. Some fine details of the velocity cycle depend upon the reference depth, but the major features described here do not. A temperature profile from a simultaneous CTD cast is plotted in the background, and the wind stress is included as the topmost, dashed vector. Wind stress changed direction slightly on day 131, but the magnitude was roughly constant at about 0.08 N m^{-2}.

The velocity cycle is shown beginning at 0600 LT on day 131 (topmost panel of Figure 4, time increases clockwise around the figure), with a mixed layer of about 35 m thickness. By the next panel at 1000 LT, some heating has occurred and a warm surface layer has begun to form. Note that the momentum flux supplied by the wind stress appears to be surface trapped over a depth scale that is very similar to that for the heat flux. The result is a surface half-jet, or diurnal jet, in the upper ocean velocity profile (*Strass* [1983] and *Woods and Strass* [1986] have applied the term diurnal jet to the flow just beneath the surface current we describe here). During the morning the diurnal jet accelerates parallel to the wind stress. Its amplitude reaches a maximum in early afternoon of typically $V_s' \simeq 0.1$ m s^{-1}. The diurnal jet is constantly being rotated cum sole by the Coriolis force, and by sunset it is almost perpendicular to the wind stress. Further rotation causes the diurnal jet to turn up into the wind, and by sunrise of the next morning the diurnal jet is nearly erased by the same wind stress which created it during the previous day.

6.3. *Coupling of the Thermal and Velocity Cycles*

Some kind of diurnal thermal and velocity cycle occur on each day of this experiment, though their amplitude and vertical structure can vary a good deal from day to day. To begin to see this we have plotted the full VMCM record in the form of the temperature difference and vector velocity difference between 2 m and 25 m (Figure 5) along with the model solution. Dashed lines are superposed at 1400 LT on each day. As was discussed in section 2, differencing two near-surface levels will serve to suppress somewhat the effects of horizontal advection, but even so there remain other competing phenomena which partially obscure the diurnal cycle. There are at least two instances of temperature inversions which appear to be genuine, days 135–136 and 140–141 (these suggest that salinity must have been important at least intermittently but was not measured by VMCMs), and also higher-frequency inversions which may be measurement noise (VMCM least count, Table 1). Further, 25 m is too shallow to be an appropriate reference level for calculating anomalies, and hence these differences will be referred to as stratification and shear (but not normalized by the depth interval). Even with these drawbacks, the full record serves to make two important points.

First, on almost every day both the stratification and shear go through a distinct maximum at about 1400 LT, the time when the surface amplitude of the diurnal cycle is usually a maximum, and then go through a minimum in the early

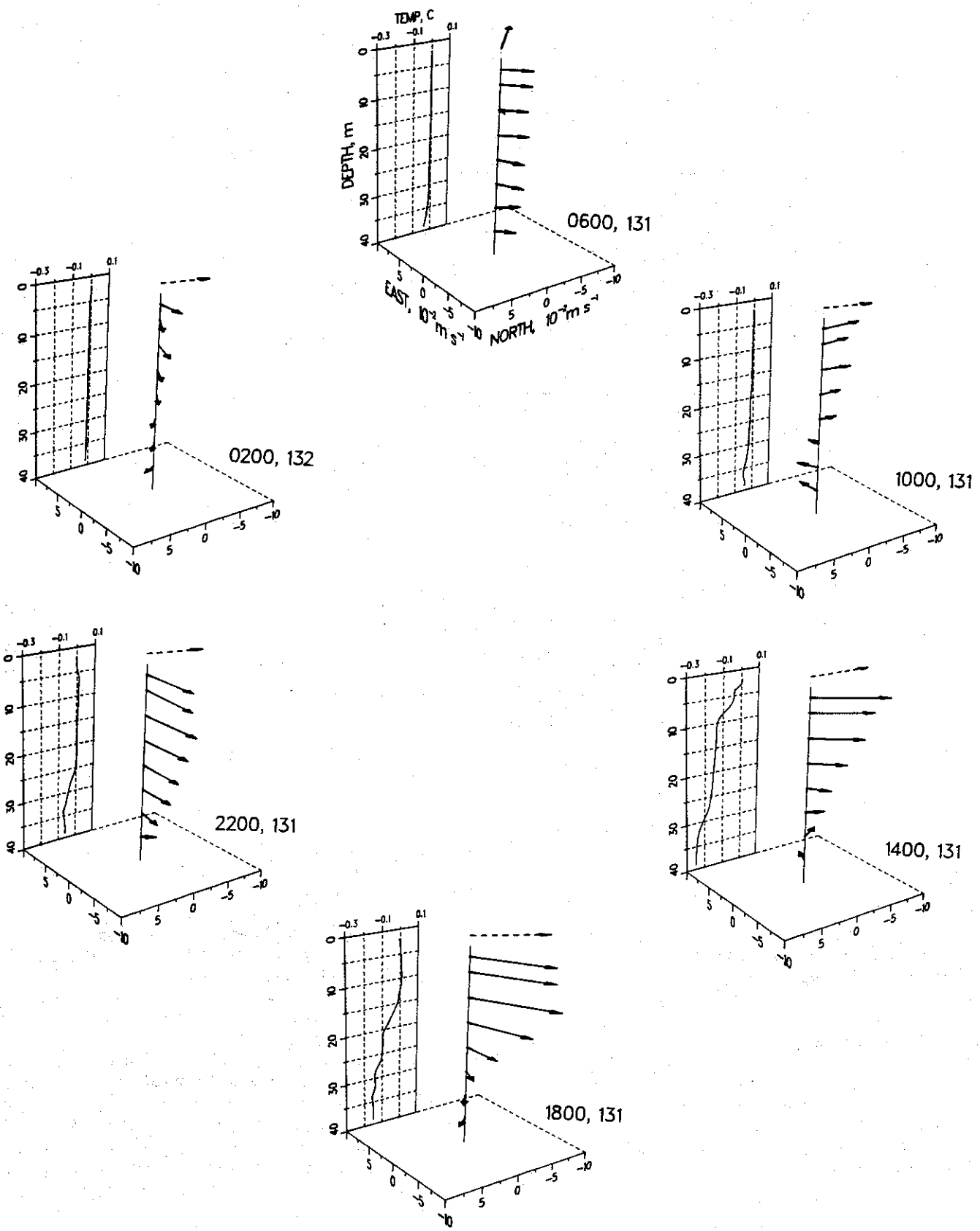

Fig. 4. Diurnal velocity cycle observed on day 131. The VMCM-measured velocity is referenced to 40 m. The topmost dashed vector is the wind stress, and the temperature profile is plotted in the background. Local time and day are marked on the lower right in each panel.

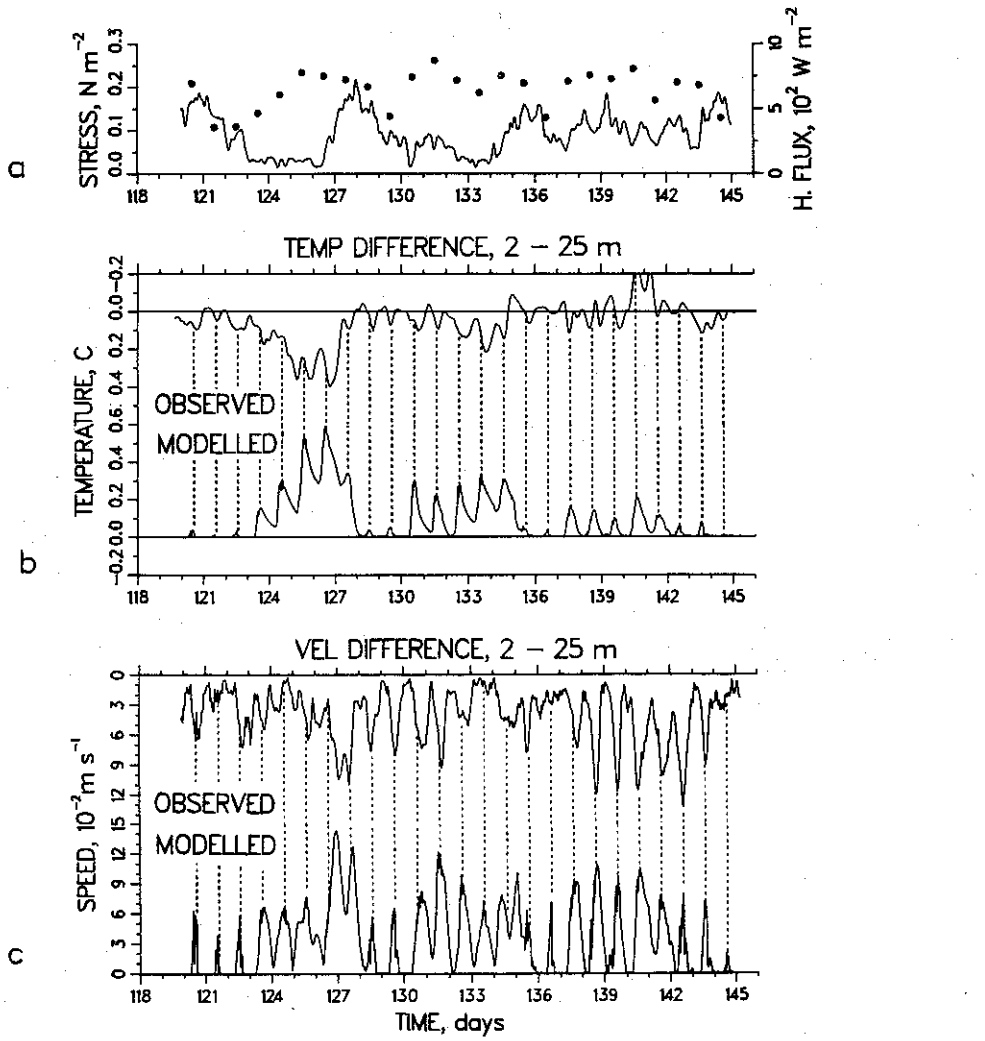

Fig. 5. The full record of temperature and velocity differences. (*a*) Wind stress amplitude and daily maximum surface heat flux (dots). (*b*) Temperature difference from 2 to 25 m observed by VMCMs (top) and modeled (bottom). (*c*) Velocity difference as above. The dotted lines are at 1400 LT each day.

morning when the temperature and velocity mixed layers reach below 25 m. This daily modulation of the upper ocean shear shows the crucial role that heating and stratification must play in setting the vertical structure of the time-averaged wind-driven velocity (more on this in section 8).

Second, there is very large day-to-day variability in the amplitude of the stratification and shear, and there is some evidence that they covary. During a period of very light winds and strong heating, days 125–127, the midday maxima were especially large in both stratification and shear. During the two days with the heaviest winds and lightest heating, days 121 and 144, the maxima in stratification and shear were quite weak. Thus the vertical shear of the wind-driven velocity displays a dependence upon wind stress amplitude that can be just opposite that of a classical wall layer or Ekman layer. How this happens is taken up in the next section, where we examine the parameter dependence of the diurnal cycle.

7. Parameter Dependence and Model Results

7.1. *Thermal Cycle*

Most of the day-to-day variability in the diurnal thermal cycle found in this data set is due to the variations of wind stress magnitude. This may be seen in a qualitative way in the VMCM record of Figure 1*c*; the days with the smallest T_s response (days 121–122 [roughly 0.05°C], 128–129, and 135–136) are the days with the largest wind stress, while the days with the largest response (days 123–126 [roughly 0.4°C] and 135–136) are the days with the smallest wind stress. The important role of wind mixing under these moderate, fair weather conditions has been observed before [*Sverdrup et al.*, 1942; *Hoeber*, 1972; *Pollard*, 1977; *Kondo et al.*, 1979; *Simpson and Dickey*, 1981].

To assess the quantitative effect of wind stress and heating variations, we limit our view to days 128–131, which the heat budget showed were relatively untroubled by horizontal advection (Figure 1*d*). The CTD data and the model solution from these four days are shown as profiles in Figures 6*c* and 6*d* and as time series of temperature at fixed depths in Figures 7*c* and 7*d*. There are advective effects evident even here: note that the observed 30-m temperature (Figure 7*c*) is more variable than the modeled 30-m temperature and shows a cooling trend not found in the model. The diurnal cycle signal is easily seen, however, and the high-resolution CTD data make it possible to calculate the trapping depth (Figure 6*e*) and the penetration depth (Figure 7*e*) from (1) and (2). These 4 days span a fairly wide range of maximum heating and wind stress (Table 2), and the diurnal cycle varies considerably over this period (recall also Figure 2).

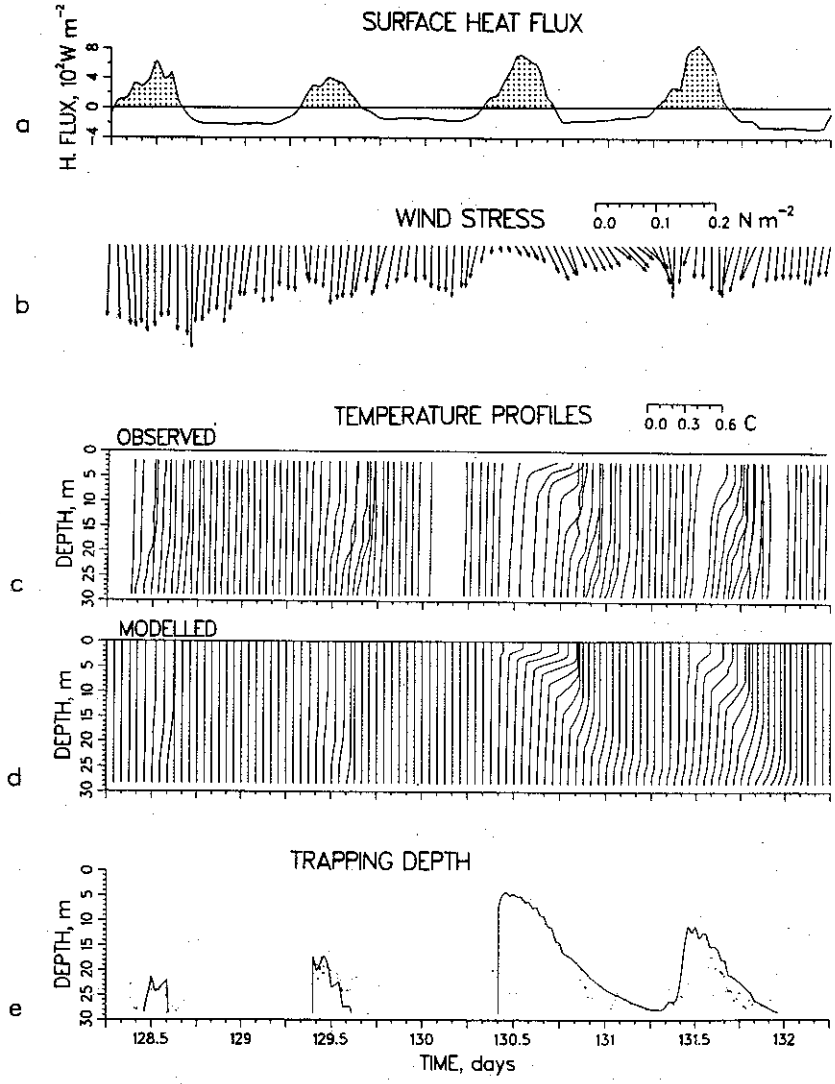

Fig. 6. CTD and model data from the period from day 128 to day 131. (*a*) Air-sea heat flux. (*b*) Wind stress. (*c*) CTD-measured temperature profiles. Note that the upper 2 m was not sampled. (*d*) Model-computed profiles. (*e*) Trapping depth calculated from individual CTD profiles (one dot per profile), and from the model data (solid curves).

We can see the effect of τ variation by comparing days 128 and 130, which have roughly equal Q, while τ on day 128 was about a factor of 4 larger than τ on day 130. The result was that $\tilde{D}_T$ on day 128 was about a factor of 4 larger than that on day 130, or roughly proportional to the ratio of wind stresses; $\tilde{T}_s$ on day 128 was about a factor of 4 smaller than that on day 130, or inversely proportional to the ratio of wind stresses. The scaling analysis (equations (16) and (17)) is consistent with this observed τ dependence.

We can see the effect of Q variation by comparing days 129 and 131, which have roughly equal τ, while Q on day 131 was approximately twice that on day 129 (owing mainly to increased cloud cover on 129). Doubled Q causes both a smaller $\tilde{D}_T$ (a little less than a factor of 2) and a larger $\tilde{T}_s$ (a little more than a factor of 2). The scaling analysis (equations (16) and (17)) is also consistent with this Q dependence.

The numerical model gives a fairly faithful simulation of the overall structure and amplitude of the diurnal cycle on these 4 days. The model-computed amplitudes and the trapping depth (and to a lesser degree, the penetration depth) show no obvious bias, suggesting that the model does roughly enough wind mixing. The model solution also reproduces well the asymmetry of the surface thermal response noted in section 6.1. Most importantly, the model simulates well the day-to-day variability of the diurnal cycle, which also suggests that the model has a parameter dependence consistent with these data. These results are encouraging, but comparison with a more extensive and less complicated (by nonlocal phenomenon) data set would be required to reach any stronger conclusion. (See *Stramma et al.* [1986] for a comparison against a somewhat larger data set spanning a much wider range of conditions.)

The simple scale estimates (Appendix B) listed in Table 2 also make fairly good predictors of $\tilde{T}_s$ and $\tilde{D}_T$. For some purposes, say, estimating the day-to-day variation of the ratio of photic zone depth to the wind-mixing depth [*Marra and Heinemann*, 1982] or forecasting the diurnal cycle [*Clancy and Pollack*, 1983], these scale estimates may be as useful as the full numerical model solution and of course are much easier to evaluate.

7.2. *Diurnal Jet Amplitude*

A diurnal jet of the sort described in section 6.2 will occur in any upper ocean model which assumes that heat and mo-

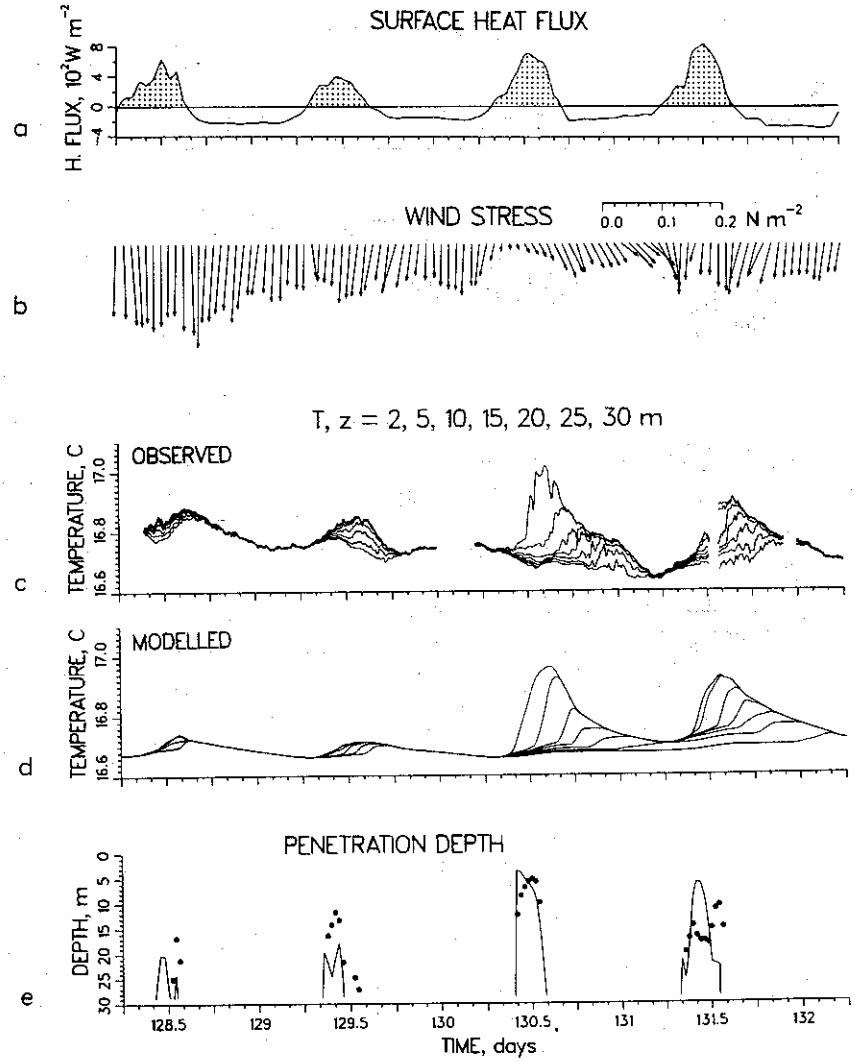

Fig. 7. CTD and model data from the period from day 128 to day 131. (*a*) Air-sea heat flux. (*b*) Wind stress. (*c*) CTD-measured temperature time series at depths of 2, 5, 10, 25, and 30 m. (*d*) Model-computed temperature time series. (*e*) Penetration depth calculated from the CTD data (heavy dots) and from the model data (solid curves).

mentum are mixed in a more or less similar way [*Kondo et al.*, 1979; *Woods and Strass*, 1986]. The amplitude and parametric dependence of the diurnal jet will, however, vary from model to model depending upon the wind-mixing mechanism and parameterization.

An at first curious result of the scaling analysis of our model (section 5) was that the diurnal jet amplitude was found to scale as

$$\tilde{V}_s \sim Q^{1/2}$$

Explicit dependence upon τ vanishes because while δV goes like τ/D_T, the trapping depth D_T is itself proportional to $\tau/Q^{1/2}$. Variations of wind stress alone are thus expected to cause variations in the thickness of the diurnal jet rather than in the amplitude.

Some evidence of this may be seen in Figure 8, which shows the magnitude of the velocity referenced to 40 m for days 128–131. The daily peaks of this velocity make rough estimates of $\tilde{V}_s'$ uncertain to about 0.02 m s^{-1} because of uncertainty in the reference level. Though τ varies by about a factor of 4 from day 128 to day 130, the diurnal jet amplitude varies from only about 0.12 m s^{-1} to 0.10 m s^{-1}. Note that days with the larger τ, 129 and especially 128, have a comparatively thick diurnal jet. This is consistent with the day-to-day variation of $\tilde{D}_T$ already noted for the thermal response and with the τ variation expected from the scaling analysis. We might have expected to see a weak dependence of $\tilde{V}_s$ upon Q and

TABLE 2. Diurnal Cycle Parameters and Scales for Days 128–131

	Day 128	Day 129	Day 130	Day 131
		Parameters		
τ, N m^{-2}	0.13	0.07	0.03	0.07
I, W m^{-2}	829	552	833	978
L, W m^{-2}	−195	−144	−105	−126
Q, W m^{-2}	634	408	728	852
P_Q, day	0.20	0.19	0.20	0.22
P_τ, day	0.18	0.17	0.19	0.20
		*Scale Estimates**		
$\tilde{T}_s$, °C	0.09	0.07	0.36	0.25
$\tilde{D}_T$, m	19	15	6	10
$\tilde{V}_s$, m s^{-1}	0.10	0.07	0.10	0.11
		Observed†		
$\tilde{T}_s'$, °C	0.08 ± 0.02	0.10 ± 0.02	0.34 ± 0.04	0.22 ± 0.02
$\tilde{D}_T$, m	21 ± 2	16 ± 2	5 ± 1	9 ± 1
$\tilde{V}_s'$, m s^{-1}	0.12 ± 0.02	0.11 ± 0.02	0.10 ± 0.02	0.10 ± 0.02

*Made from the formulae in Appendix B.
†Eyeball estimates from Figures 7, 6, and 8.

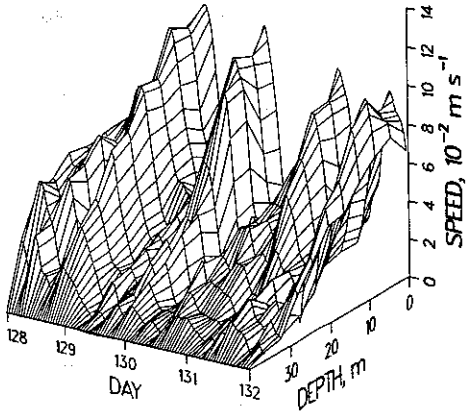

Fig. 8. Magnitude of the vector velocity difference from 40 m as a function of depth and time for the period from day 128 to day 131. The daily maximum values are reasonably good estimates of the diurnal jet amplitude.

thus a slightly larger $\tilde{V}_s$ on 130 than on 128. This weak Q dependence is not apparent in Figure 8.

7.3. *Profile Structure*

During many afternoons the temperature and velocity profiles develop a fairly clear-cut two-layer structure with a surface mixed layer above a stratified and sheared transition layer (Figures 4 and 6). Temperature mixed layers are a very familiar feature in ocean data and are often built into upper ocean models (including ours; see also *Niiler and Kraus* [1977] and *Garwood* [1979]). It is particularly striking that on day 128 a surface mixed layer of at least 10-m thickness persisted right through the day despite strong heating (best seen in the time series of Figure 7*c*). Models which assume that fluxes are proportional to the local vertical gradient times a diffusivity [e.g., *Kondo et al.* [1979] or the "gradient mixing only" solution of Appendix A) tend to develop substantial near-surface gradients under these conditions. In this respect they may be less realistic than simpler mixed-layer models which take a surface mixed-layer for granted.

These data show that a velocity surface mixed layer is also present and is at least roughly coincident with the temperature mixed layer. For example, a velocity mixed layer of about 30-m thickness exists at 0600 LT on day 131 (Figure 4), coincident with the temperature mixed layer, even though the mixed layer was absorbing a stress of about 0.08 N m^{-2}. The velocity mixed layer seems to disappear during midday when near-surface stratification develops as part of the diurnal thermal cycle (that it disappears depends on the vertical sampling interval) and then reappears along with the temperature mixed layer at 1800 LT on day 131. At that time the surface mixed layer was absorbing both a surface stress of about 0.08 N m^{-2} as well as an entrainment stress, and again there is little sustained vertical shear of velocity within the temperature mixed layer (no more than about 10^{-3} s^{-1}). Some process which we can not directly identify in these data, perhaps large-scale eddies like Langmuir circulations [*Weller et al.*, 1986], must be acting to overturn the mixed layer within tens of minutes. On days with stronger winds, the velocity mixed layer may remain deep right through the day, just as we noted above for the temperature mixed layer. Thus stronger winds may produce (contrary to intuition and to classical theories which ignore stratification altogether) reduced shear between fixed levels in the upper ocean (section 6.3).

Our model produces a realistic profile structure because we built in a surface mixed layer at the outset (thickness is given by (9)) and allowed for a smooth transition layer by admitting mixing below the mixed layer (according to (10)). During midday, when the transition layer is thickest, active vertical mixing occurs through only about the upper half of the model's transition layer, while the lower half is quiescent. The density difference $\Delta\rho$ felt by the bulk Richardson number condition (equation (9)) will then be less than the surface density anomaly $\delta\rho$, and the gradient Richardson number averaged across the full transition layer will be somewhat greater than the critical value at which active mixing begins. Sometime after sunset, once surface heat loss has reduced the heat anomaly of the diurnal layer, vertical mixing will usually be active through the full depth of the transition layer, and then the criticality condition on the Richardson numbers may be checked against the observations using the easily observed surface anomalies. For example, at 1800 LT on day 131 (Figure 4) there is a velocity change of about 0.1 m s^{-1} (the full amplitude of the diurnal jet) over a 10-m-thick transition layer (15 to 25 m) across which the temperature change is roughly 0.1°C (density change of about 0.023 kg m^{-3}). These

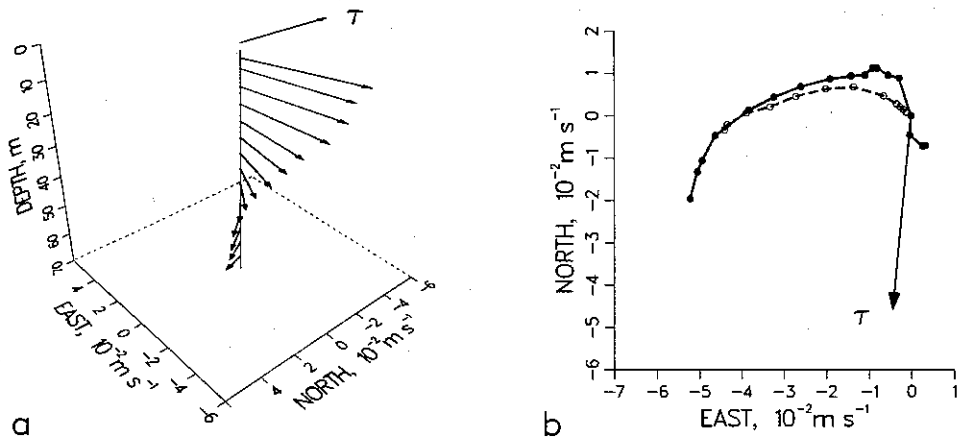

Fig. 9. Time-averaged velocity for the period from day 120 to day 145. (*a*) VMCM-measured velocity, referenced to 70 m. The topmost vector is the time-averaged wind stress. (*b*) Hodograph plots of the observed (solid curve) and model-computed (dashed curve) time-averaged velocity. Depth is shown by symbols every 4 m, starting from 2 m. In both cases the zero or reference velocity has been placed at 70 m.

give $R_g \sim \frac{1}{4}$ (averaged across the transition layer) and $R_b \sim \frac{1}{2}$ (mixed-layer depth measured to the middle of the transition layer is 20 m), or grossly consistent with the values assumed in the model. This shows too that what would seem to be a very small temperature difference, 0.1°C, can sustain the full diurnal jet, consistent with the R_g condition. Thus even very weak stratification may be crucially important in determining the vertical structure of the wind-driven velocity.

8. The Time-Averaged Response

8.1. *Velocity Spiral*

We have seen in the two previous sections that in fair weather conditions the instantaneous, wind-driven, upper ocean velocity is usually dominated by the diurnal jet. Not surprisingly then, the time-averaged, wind-driven velocity (Figure 9*a*) has a spiral structure which can best be understood as a product of diurnal cycling (imagine taking the time average over the diurnal velocity cycle of Figure 4). The time-averaged velocity is surface intensified, as is the diurnal jet, and the near-surface velocity points well to the right (cum sole) of the time-averaged wind stress ($\approx 60°$). The time-averaged velocity decreases and turns to the right with increasing depth because the diurnal jet decays and turns to the right as it penetrates deeper into the water column during early evening.

At first glance this observed spiral resembles an Ekman spiral, but there are important differences in the structure and rather profound differences in the dynamics. Compared with an Ekman spiral, this spiral is rather flat in that the velocity amplitude decays with depth considerably faster than the velocity vector rotates to the right with depth (noted too by *Weller* [1981]). But more important, the vertical shear of the wind-driven velocity is closely tied to stratification, which is altogether ignored in the classical Ekman theory. In the absence of heating and the resulting stable stratification, for example in the nighttime mixed layer, there is only very weak vertical shear and certainly no spiral of the sort found on average over one or several diurnal cycles. On the other hand, if the heating had been stronger or the wind stress weaker, then it can be anticipated that the velocity spiral would have been more strongly surface trapped (recall the differences between days 128 and 130 seen in Figure 8).

A velocity spiral of this kind should be present in the time average whenever the upper ocean is undergoing diurnal cycling. We suggest that it be termed the "diurnal cycle spiral" to distinguish it from the classical Ekman spiral and to emphasize the vital role of heating and stratification.

8.2. *Transport*

It is well known that the wind-driven mass transport is independent of the form of vertical mixing or the structure of the velocity spiral. If no forces other than wind stress and rotation act upon the water column, then aside from sampling errors the observed transport,

$$(M_x, M_y)_{z_r} = \int_{z_r}^{0} (\bar{U}, \bar{V})\, dz$$

should equal the Ekman transport,

$$\frac{1}{f_{\rho_0}} (-\bar{\tau}_y, \bar{\tau}_x)$$

where the time-averaged wind stress in this case is

$$(\bar{\tau}_x, \bar{\tau}_y) = (-0.008, -0.087) \text{ N m}^{-2}$$

and z_r is the reference depth. Transports estimated from the data, the Ekman transport, and the model transport are

	M_x	M_y
observed, $z_r = 50$ m	−0.9	0.4
observed, $z_r = 70$ m	−1.6	0.2
modeled	−1.0	0.1
Ekman	−1.0	0.1

where M_x and M_y are in square meters per second. When estimating transport from the observations, we have taken the reference depth z_r to be 50 m, which has below the mixed-layer depth at most times during the experiment, and alternatively 70 m, which was deeper than the mixed layer at any time. It could be argued that either of these reference depths is appropriate, and hence the difference in transport is a measure of the uncertainty of the estimate.

Transport computed from the time-averaged velocity of the model is, trivially, the same as the Ekman transport. On the other hand, the transport estimated from the observations differs from Ekman transport by up to 50% (using $z_r = 70$ m). We suspect that the discrepancy between the observed transport and Ekman transport arises mainly from a thermal wind contribution to the time-averaged shear, but we cannot verify this with the available data.

8.3. *Fluxes*

While we are unable to say anything very definite about the magnitude of the observed transport, we have learned that in fair weather conditions the process of diurnal cycling determines how deeply the wind-driven transport penetrates the upper ocean and thus determines which water makes up the Ekman transport. Figure 4 shows that the fastest flowing part of the diurnal jet (during early afternoon) is also the warmest water in the diurnal thermal cycle. The result is a persistent velocity-temperature correlation and a resulting "eddy" heat flux over and above the heat flux due to the time-average transport. In this case the additional heat flux is roughly

$$\rho_0 c \int_{50}^{0} (\overline{U'T'}, \overline{V'T'})\, dz \sim (0, -3) \times 10^6 \text{ W m}^{-1}$$

(which is small by most standards) and is nearly parallel to the time-averaged wind stress. Advection by the diurnal jet can be expected to produce an enhanced horizontal transport of any property which has a diurnal depth dependence, e.g., perhaps some phytoplankton species. (A similar kind of temperature-velocity correlation and eddy heat flux might be expected over an annual cycle.)

9. Conclusions and Remarks

1. The diurnal cycle is an important mode of fair weather variability which arises when solar heating stabilizes the surface layer and causes the surface fluxes of heat and momentum to be surface trapped during midday. Heat and momentum fluxes appear to be mixed in a similar way, so that the thermal and velocity cycles are closely coupled. Temperature and velocity profiles observed during the afternoon often show a two-layer structure, with coincident temperature and velocity surface mixed layers overlying a thick, stratified and sheared transition layer.

2. We have modeled the diurnal cycle with a very simple mixed-layer model which allows for mixing in the stratified fluid below the mixed layer. This model gives quite realistic

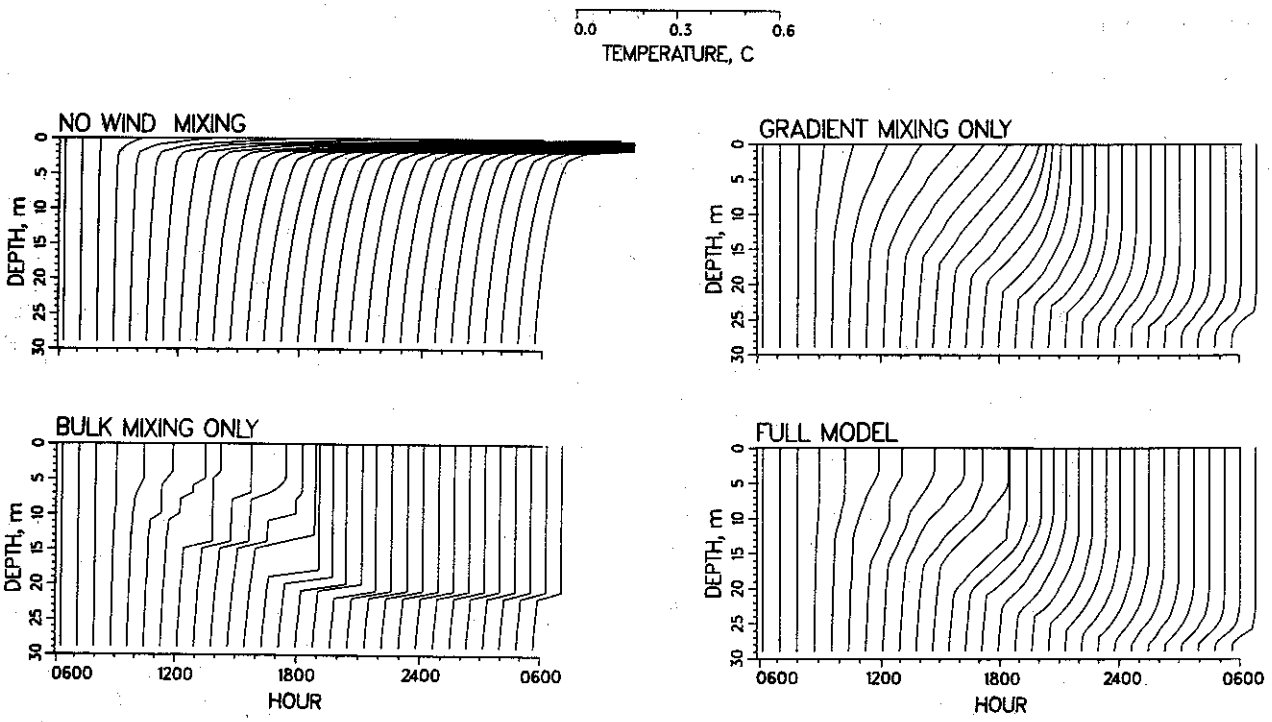

Fig. 10. Mixing experiments run using the numerical model with one or both wind-mixing processes shut off for comparison to the full model (lower right).

profile structures and has some success simulating the amplitude and day-to-day variability of the diurnal cycle.

3. Our model presumes that wind-mixing is a consequence of shear flow instability. In that event, the trapping depth of the thermal and velocity response is proportional to $\tau/Q^{1/2}$, perhaps the most important result of this paper. It follows that the thermal response is proportional to $Q^{3/2}/\tau$ and that the diurnal jet amplitude is proportional to $Q^{1/2}$. These are consistent with our observations but require testing against a larger and less complicated data set than was available here.

4. The time-averaged profile of wind-driven velocity which makes up the Ekman transport has a flat, spiral shape as a direct consequence of diurnal cycling. In this regard at least, the process of diurnal cycle plays an important role in shaping the long-term response of the upper ocean to atmospheric forcing.

APPENDIX A: MIXING EXPERIMENTS

To see the consequences of the three mixing processes identified in our model (section 4), i.e., (1) free convection, (2) mixed-layer entrainment, and (3) shear flow instability, we have carried out some very simple numerical experiments in which we arbitrarily shut off one or both of the wind-mixing processes, (process 2 and/or 3). These experiments are run using idealized forcing (steady wind stress, steady heat loss, and sinusoidal insolation) whose values are approximately those of day 131: $I = 980$ W m^{-2}, $L = -125$ W m^{-2}, $P_Q = 5$ hours, and $\tau = 0.07$ N m^{-2}. The observed diurnal thermal cycle on day 131 had a response (Table 2) of $D_T = 9$ m and $T_s = 0.22$°C, which can serve as a guide to reasonable values.

A1. *Free Convection Only*

Wind mixing may be shut off in the model by setting both R_b and R_g to zero. Vertical mixing by free convection will then occur only down to the convection depth, which for these parameters is very shallow, roughly $\frac{1}{2}$ m during midday. Thus without wind mixing, the thermal response is very strongly surface trapped and its surface amplitude is extremely large (Figure 10); $\tilde{D}_T = 1.5$ m, and $\tilde{T}_s = 1.6$°C. This very unrealistic simulation demonstrates the crucial role that wind mixing must have played on this day in distributing heat through a much thicker surface layer than can be reached by convective processes and direct radiation absorption alone. (When the wind nearly dies [e.g., *Halpern and Reed*, 1976; *Stramma et al.*, 1986], then this radiation/convection envisioned by *Kraus and Rooth* [1961] and *Dalu and Purini* [1981] will obtain.]

A2. *Mixed-Layer Entrainment Only*

With R_g set to zero the model reduces exactly to the conventional, bulk mixed-layer model DIM of *Price et al.*, [1978] (see also *Pollard et al.*, [1973]). This model gives a reasonable account of wind mixing in an overall sense and thus gives a good account of the surface response: $\tilde{D}_T = 10$ m, and $\tilde{T}_s = 0.23$°C. However, the profile shape given by this model is grossly unrealistic in a way that is characteristic of all mixed-layer models [e.g., *Denman*, 1973]: in place of the smooth, thick transition layer found at the base of the oceanic mixed layer, there is instead an abrupt jump whose thickness is just the grid interval. For problems in which the profile shape is important, i.e., acoustic propagation or heat budgeting, then a conventional, bulk mixed-layer model may be too severe an idealization.

A3. *Gradient Mixing Only*

With R_b set to zero the model mixes locally the density and velocity profiles just enough to satisfy the shear flow stability criterion that the gradient Richardson number should be no larger than $\frac{1}{4}$. This too gives a fairly reasonable account of vertical mixing in an overall sense: $\tilde{D}_T = 8$ m, and $\tilde{T}_s = 0.27$°C. But now the profile structure is unrealistic in a way

that just complements the bulk mixed-layer model noted above. This model can not produce a surface mixed layer by wind mixing alone; a surface mixed layer develops only after sunset by the free convection process. The field data on the other hand, show that a well-defined temperature and velocity mixed layer can persist through the day provided that the wind stress does not vanish.

A4. *Full Model*

With both wind-mixing processes acting at once, the model-simulated profile develops a two-layer structure which is qualitatively like that observed in the ocean. There is a surface mixed layer which is as thin as 4 m near noon, bounded below by a smooth transition layer whose thickness is roughly 20 m near noon. In the full model the task of satisfying the stability criterion by means of wind mixing is shared between the two Richardson number criteria, and the net result is about as much wind mixing as occurs by the mixed-layer entrainment process alone: $\tilde{D}_T = 9$ m, and $\tilde{T}_s = 0.21$°C. To the extent that the profile structure matters (rather than just the surface response), the full model is clearly preferable to the conventional mixed-layer model or to the gradient-mixing model.

APPENDIX B: FURTHER DEVELOPMENT OF THE SCALING ANALYSIS

By a fairly straightforward extension of the scaling analysis we can derive a complete, accurate, closed form "solution" for $\tilde{D}_s$, $\tilde{T}_s$, and $\tilde{V}_s$. To do this, we have to account for the effects of radiation absorption at depth, find the constants needed to make equalities, and lastly, consider how the physics must change in the limit of vanishing τ.

B1. *Radiation Absorption*

When the absorption of insolation is considered, then a dimensional analysis gives that each of (16)–(18) must be multiplied by some function $J(D_T/\lambda_2)$, where recall λ_2 is the shortwave extinction scale of (6). Inspection of (6) together with trial and error have given a form of J.

$$J(D_T/\lambda_2) = \left[1 - I_2 \frac{I - L}{I} \exp(-D_T/\lambda_2)\right] \tag{19}$$

B2. *Calibration Against the Numerical Model*

The scaling analysis has been calibrated against solutions of the numerical model in order to find the leading constants for (16)–(18) [which were expected to be $O(1)$] and to find the best fit exponent on J. The scale estimates were first calibrated in the limit of vanishing λ_2 ($J = 1$) to find the leading constants, and then this preliminary estimate of D_T was used in J to then find the power law dependence upon J for finite λ_2. This last step of the calibration is approximate and introduces a small error, generally no more than about 10%. The end result is the wind-mixing regime form of the scaling analysis which holds throughout the range of τ and Q encountered in this study. The daily minimum trapping depth $\tilde{D}_T$ is

$$\tilde{D}_T = 0.45 \frac{\tau}{Q^{1/2}} \frac{P_\tau}{P_Q^{1/2}} \left(\frac{c}{-\alpha g}\right)^{1/2} J^{-3/2} \tag{20}$$

the range of surface temperature $\tilde{T}_s$ is

$$\tilde{T}_s = 1.5 \frac{Q^{3/2}}{\tau} \frac{P_Q^{3/2}}{P_\tau} \frac{(-\alpha g)^{1/2}}{\rho_0 c^{3/2}} J^{3/2} \tag{21}$$

and the diurnal jet amplitude $\tilde{V}_s$ is

$$V_s = 1.5\, Q^{1/2} P_Q^{1/2} \left(\frac{-\alpha g}{\rho_0^2 c}\right)^{1/2} J^{1/2} \tag{22}$$

B3. *Free Convection Limit*

In the limit of vanishing wind stress, the wind-mixing scale estimates must fail; e.g., $\tilde{T}_s$ becomes infinite. The scaling must change over to a different form, governed by free convection and radiation absorption (i.e., the no-wind-mixing case of Appendix A). The mixing depth is then the convection depth C [*Dalu and Purini*, 1981] at which the heating rate by insolation is equal to the heat absorbed above $z = C$ within a surface mixed layer, i.e.,

$$\frac{[I(0) - I(C) + L]}{C} = \left.\frac{\partial I}{\partial z}\right|_C \tag{23}$$

Given the insolation absorption profile (equation (6)), the daily minimum convection depth $\tilde{C}$ may be easily calculated from (23) given L and the daily maximum I.

As before, we presume that (13) holds, and calibration against the corresponding numerical model solution shows that the leading constant is 1.0. The effect of penetrating solar insolation has already been accounted for in C, and no J function is needed. The trapping depth may be evaluated from its definition (equation (1)), together with the known $\tilde{C}$ and $\tilde{T}_s$ and assuming that $T(z) = P_Q(\partial I/\partial z)/\rho_0 c_p$ at depths below $z = \tilde{C}$. The daily minimum trapping depth $\tilde{D}_T$ is

$$\tilde{D}_T = \tilde{C} + \frac{I(\tilde{C})}{\tilde{T}_s} \frac{P_Q}{\rho_0 c} \tag{24}$$

the range of surface temperature $\tilde{T}_s$ is

$$\tilde{T}_s = \frac{I(0) - I(\tilde{C}) + L}{\tilde{C}} \frac{P_Q}{\rho_0 c} \tag{25}$$

and the diurnal jet amplitude $\tilde{V}_s$ is

$$\tilde{V}_s = \frac{\tau}{\tilde{C}} \frac{P_\tau}{\rho_0} \tag{26}$$

B4. *Choosing the Scaling*

To find which form of the scaling holds for a given τ and Q, we calculate both forms and then compare the two estimates of $\tilde{D}_T$. The deeper value invariably conforms to the numerical model result. For example, if the free convection $\tilde{D}_T$ is found to be less than the wind-mixing $\tilde{D}_T$, then wind mixing would have dominated for those conditions, and the wind-mixing scaling obtains. This gives the result of selecting always the smaller $\tilde{T}_s$ and $\tilde{V}_s$.

These scale estimates make an easily evaluated proxy for the full numerical model and also serve to show the explicit dependence upon all of the important known external variables. We caution though that they have been derived under somewhat restrictive conditions, and may not be accurate if conditions differ too strongly from those assumed (e.g., steady wind).

Acknowledgments. We are grateful to the Office of Naval Research for their support of this program through contract N00014-76-C-0197, NR 083-400 with the Woods Hole Oceanographic Institution, (R. A. W. and J. F. P.) and contract N00014-75-C-0152 with Scripps Institution of Oceanography (R. A. W.). Development and operation of the CTD system was funded through the Office of Naval Research

code 200 and code 220 and Naval Ocean Research and Development Activity code 540 (R. P.). We thank R. Michael Clancy, Pijush K. Kundu, Paul J. Martin, and the referees for their helpful comments on this paper. Woods Hole Oceanographic Institution contribution 5427.

REFERENCES

Adamec, D., R. L. Elsberry, R. W. Garwood, and R. L. Haney, An embedded mixed-layer-ocean circulation model, *Dyn. Atmos. Oceans*, *6*(2), 69–96, 1981.

Bruce, J. G., and E. Firing, Temperature measurements in the upper 10 m with modified expendable bathythermograph probes, *Journal of J. Geophys. Res.*, *79*, 4110–4111, 1974.

Clancy, R. M., and K. O. Pollack, A real-time synoptic ocean thermal analysis/forecast system, *Prog. Oceanogr. 12*, 383–424, 1983.

Dalu, G. A., and R. Purini, The diurnal thermocline due to buoyant convection, *Q. J. R. Meteorol. Soc.*, *108*, 929–935, 1981.

Davis, R. E., R. DeSzoeke, D. Halpern, and P. Niiler, Variability in the upper ocean during MILE, I, The heat and momentum balances, *Deep Sea Res.*, *28*, 1427–1451, 1981.

Deardorff, J. W., A. E. Willis, and D. K. Lilly, Laboratory investigation of nonsteady penetrative convection, *J. Fluid Mech.*, *35*, 7–31, 1969.

Denman, K. L., A time-dependent model of the upper ocean, *J. Phys. Oceanogr.*, *3*, 173–184, 1973.

Dickey, T. D., and J. J. Simpson, The influence of optical water type on the diurnal response of the upper ocean, *Tellus, Ser. B*, *35*, 142–154, 1983.

Garwood, R. W., Jr., Air-sea interaction and dynamics of the surface mixed layer, *Rev. Geophys.*, *17*, 1507–1524, 1979.

Gill, A. E., *Atmosphere-Ocean Dynamics*, 662 pp., Academic, Orlando, Fla., 1982.

Gill, A. E., and J. S. Turner, A comparison of seasonal thermocline models with observation, *Deep Sea Res.*, *23*, 391–401, 1976.

Halpern, D., and R. K. Reed, Heat budget of the upper ocean under light winds, *J. Phys. Oceanogr.*, *6*, 972–975, 1976.

Hoeber, H., Eddy thermal conductivity in the upper 12 m of the tropical Atlantic, *J. Phys. Oceanogr.*, *2*, 303–304, 1972.

Imberger, J., The diurnal mixed layer, *Limnol. Oceanogr.*, *30*, 737–770, 1985.

Kondo, J., Y. Sasano, and T. Ishii, On wind-driven current and temperature profiles with diurnal period in the oceanic planetary boundary layer, *J. Phys. Oceanogr.*, *9*, 360–32, 1979.

Kraus, E. B., *Atmosphere-Ocean Interaction*, Press, 275 pp., Clarendon, Oxford, England, 1972.

Kraus, E. B., and C. Rooth, Temperature and steady state vertical heat flux in the ocean surface layers, *Tellus*, *2*, 231–238, 1961.

Kronenburg, C., Wind-induced entrainment in a stably stratified fluid, *J. Fluid Mech.*, *145*, 253–273, 1985.

Large, W. G., and S. Pond, Open ocean momentum flux measurements in moderate to strong winds, *J. Phys. Oceangr.*, *11*, 324–336, 1981.

Large, W. G., and S. Pond, Sensible and latent heat flux measurements over the ocean, *J. Phys. Oceanogr.*, *12*, 464–482, 1982.

Lynn, R. J., and J. Svejkovsky, Remotely sensed sea surface temperature variability off California during a "Santa Ana" clearing, *J. Geophys. Res.*, *89*, 8151–8162, 1984.

Marra, J., and K. Heinemann, Photosynthesis response by phytoplankton to sunlight variability, *Limnol. Oceanogr.*, *27*(6), 1141–1153, 1982.

Martin, P. J., Testing and comparison of several mixed-layer models, Tech. Rep., 23 pp., Nav. Ocean Res. and Develop., Natl. Space Technol. Lab., Miss., 1986.

Mellor, G. L., and P. A. Durbin, The structure and dynamics of the ocean surface layer, *J. Phys. Oceanogr.*, *5*, 718–728, 1975.

Montgomery, R. B., and E. D. Stroup, Equatorial waters and currents at 150°W in July–August 1952, *Johns Hopkins Oceanogr. Stud.*, *1*, 68 pp., 1962.

Niiler, P. P., and E. B. Kraus, One-dimensional models, in *Modeling and Prediction of the Upper Layers of the Ocean*, edited by E. B. Kraus, pp. 143–172, Pergamon, New York, 1977.

Paulson, C. A., and J. J. Simpson, Irradiance measurements in the upper ocean, *J. Phys. Oceanogr.*, *7*, 952–956, 1977.

Phillips, O. M., *The Dynamics of the Upper Ocean*, 336 pp., Cambridge University Press, New York, 1977.

Pinkel, R., Upper ocean internal wave observations from FLIP, *J. Geophys. Res.*, *80*, 3892–3910, 1975.

Pinkel, R., Doppler sonar observations of internal waves: Wavefield structure, *J. Phys. Oceanogr.*, *13*, 804–815, 1983.

Pollard, R. T., Observations and models of the structure of the upper ocean, in *Modeling and Prediction of the Upper Layers of the Ocean*, Edited by E. B. Kraus, pp. 102–117, Pergamon, New York, 1977.

Pollard, R. T., P. B. Rhines, and R. O. R. Y. Thompson The deepening of the wind-mixed layer, *Geophys. Fluid Dyn.*, *4*, 381–404, 1973.

Price, J. F., Observations of a rain-formed mixed layer, *J. Phys. Oceanogr.*, *9*, 643–649, 1979.

Price, J. F., C. N. K. Mooers, and J. C. Van Leer, Observation and simulation of storm-induced mixed-layer deepening, *J. Phys. Oceanogr.*, *8*, 582–599, 1978.

Rubenstein, D. M., The daytime evolution of the East African jet, *J. Atmos. Sci.*, *38*, 114–128, 1981.

Simpson, J. J., and T. D. Dickey, Alternative parameterizations of downward irradiance and their dynamical significance, *J. Phys. Oceanogr.*, *11*, 876–882, 1981.

Soloviev, A. V., and N. V. Vershinsky, The vertical structure of the thin surface layer of the ocean under conditions of low wind speed, *Deep Sea Res.*, *29*, 1437–1449, 1982.

Stommel, H., K. Saunders, W. Simmons, and J. Cooper, Observations of the diurnal thermocline, *Deep Sea Res.*, *16*, 269–284, 1969.

Stramma, L., P. Cornillon, R. A. Weller, J. F. Price, and M. G. Briscoe, Large diurnal sea surface temperature variability: Satellite and in situ measurements, *J. Phys. Oceanogr.*, in press, 1986.

Strass, V., Ein eindimensionales numerisches Modell zum Einfluss des Tagesganges der Deckschicht auf das winderzeugte Stromprofil, Diplomarbeit, Christian-Albrechts-Univ., Kiel, Federal Republic of Germany, 1983.

Sverdrup, H. U., M. W. Johnson, R. H. Fleming, *The Oceans, Their Physics, Chemistry and Biology*, 1087 pp., Prentice Hall, Englewood Cliff, N. J., 1942.

Thompson, R. O. R. Y., Efficiency of conversion of kinetic energy to potential energy by a breaking internal gravity wave, *J. Geophys. Res.*, *85*(C11), 6631–6635, 1980.

Thorpe, S. A., and T. H. Guymer, The nocturnal jet, *Q. J. R. Meteorol. Soc.*, *103*, 633–653, 1977.

Tully, J. P., and L. F. Giovando, Seasonal temperature structure in the eastern subarctic Pacific Ocean, Marine Distributions, *Spec. Publ. 5*, pp. 10–36, R. Soc. of Can., Ottawa 1963.

Turner, J. S. *Buoyancy Effects in Fluids*, 367 pp. Cambridge University Press, New York, 1973.

Weller, R. A., Observations of the velocity response to wind forcing in the upper ocean, *J. Geophys. Res.*, *86*, 1969–1977, 1981.

Weller, R. A., Near surface velocity variability at inertial and subinertial frequencies in the vicinity of the California Current, *J. Phys. Oceanogr.*, *15*, 372–385, 1985.

Weller, R. A., and R. E. Davis, A vector measuring current meter, *Deep Sea Res.*, *27*, 565–582, 1980.

Weller, R. A., R. Pinkel, and J. F. Price, Diurnal jets (abstract), *Eos Trans. AGU.*, *64*(18), 247, 1983.

Weller, R. A., J. P. Dean, J. Marra, J. F. Price, E. A. Francis, and D. C. Boardman, Three-dimensional flow in the upper ocean, *Science*, *227*, 1552–1556, 1986.

Woods, J. D., and W. Barkmann, The response of the upper ocean to solar heating, I, The mixed-layer, *Q. J. R. Meteorol. Soc.*, in press, 1986.

Woods, J. D., and V. Strass, The response of the upper ocean to solar heating, II, The wind-driven current, *Q. J. R. Meteorol. Soc.*, in press, 1986.

R. Pinkel, Scripps Institution of Oceanography, La Jolla, CA 92093.

J. F. Price and R. A. Weller, Woods Hole Oceanographic Institution, Woods Hole, MA 02543.

(Received June 22, 1985;
accepted August 22, 1985.)